Proceedings of the 2nd International Conference on Applied Physics and Mathematical Modeling
DOI: 10.54254/2753-8818/53/20240196

Visualization of particulate matters in air using lensless microscopy

Zhi Huang

Kent School, Kent, Connecticut, USA

jessehuang3737@gmail.com

Abstract. Air quality is crucial for health, yet monitoring airborne particulate matter (PM), particularly PM2.5, remains challenging due to pollution and widespread distribution. PM2.5, with diameters less than 2.5 micrometers, are known to have significant health implications. Traditional methods of PMs detection and analysis are often time-consuming or require complex optical systems. This study explores the use of lensless microscopy as an innovative and cost-effective alternative for the visualization and measurement of PMs. Utilizing computational imaging techniques, lensless microscopy captures high-resolution images without the need for traditional lenses, facilitating rapid and accurate analysis of air quality. We describe the implementation of lensless imaging to detect and quantify PM2.5 particles in the air, highlighting the use of the single light wavelength and the computational reconstruction method. Our experiments demonstrated that this approach could effectively capture fine details of PMs, achieving resolutions comparable to traditional microscopy. This validates the potential of lensless microscopy as a practical tool for real-time air quality monitoring. By adopting lensless microscopy, we offer a more efficient and economical method for the continuous monitoring of PMs, which can significantly contribute to environmental health studies and pollution control efforts. According to specific needs, simply replacing the flow rate of the air pump can adapt to the PM measurement speed requirements in different environments. This research introduces a novel approach to air quality assessment, providing a promising solution for the rapid and detailed analysis of airborne particulate matter while at an affordable cost.

Keywords: Lensless microscopy, Particulate matter, Air quality.

1. Introduction

One of the main sources of air pollution is particulate matter (PM), which refers to suspended particles in the air [1]. According to the World Health Organization, PM2.5 (fine particulates) is a carcinogen [2], and PMs also include biologically relevant aerosols such as pollen, bacteria, and mold spores that may cause various illnesses. Measuring PM2.5 which is fine particulate matter with a diameter of less than 2.5 micrometers, is essential for numerous reasons. First and foremost, PM2.5 can penetrate deep into the human respiratory tract, reaching the lungs and even entering the bloodstream, which can lead to severe health issues, including respiratory infections, heart disease, and lung cancer. Owing to their minuscule size, these particles are not readily expelled from the body, and their accumulation can result in chronic conditions that impair vital organs [3]. Moreover, PM2.5 is a critical indicator of air pollution levels and is commonly utilized to evaluate the air quality in a region [4,5,6]. Monitoring PM2.5 enables

DOI: 10.54254/2753-8818/53/20240196

government agencies and health organizations to issue health advisories and effectively implement and assess pollution control policies [5]. It also empowers individuals to make well-informed decisions regarding outdoor activities, particularly in urban areas where these particles predominantly originate from vehicle emissions and industrial activities [7]. Ultimately, the measurement of PM2.5 is vital not only for safeguarding public health by reducing exposure to harmful air pollutants but also for informing policies and practices designed to enhance air quality and promote environmental health.

Currently, the market for monitoring particle equipment can be divided into two categories: personal equipment and institutional equipment [8]. Personal equipment is generally less expensive (usually $1000), but the serial detection method is often limited in throughput and concentration measurement range. The institutional equipment can solve the above-mentioned problems, but at the same time, it can also cause the equipment to be quite large and heavy. The specific comparison situation is shown in Table 1.

Table 1. Comparison of advantages and disadvantages of PM detection instruments.

	Personal Devices	Institutional Devices
Advantages	**Affordability:** Generally, less expensive, making them accessible for individual use.	**High Accuracy and Reliability:** These devices are usually more sophisticated and provide highly accurate readings, suitable for scientific research and regulatory compliance.
	Portability: Compact and lightweight, these devices can be easily carried around, allowing for personal monitoring in various environments.	**Comprehensive Monitoring:** Capable of detecting a wider range of particle sizes and concentrations, they are better suited for detailed environmental assessments.
	Convenience: Designed for ease of use, they enable individuals to check air quality instantly without specialized knowledge.	**Data Management:** Often equipped with better data logging and analysis capabilities, allowing for extensive data collection over time.
Disadvantages	**Limited Accuracy:** While useful for personal monitoring, these devices may not provide the precision required for regulatory or scientific data collection.	**Cost:** Significantly more expensive than personal devices, often making them inaccessible for individual use.
	Restricted Range: Typically, these devices have a limited range of detection capabilities and might not capture the full spectrum of particulate sizes.	**Size and Portability:** Generally larger and not portable, requiring a fixed installation, which limits their use to specific locations.
	Durability and Maintenance: Personal devices may require more frequent calibration and can be less durable compared to institutional devices.	**Operational Complexity:** They may require trained personnel to operate and maintain, adding to the operational costs.

Thus, while personal devices offer a convenient and economical way for individuals to monitor their immediate environment, institutional devices provide the accuracy, reliability, and comprehensiveness needed for in-depth air quality analysis and regulatory monitoring. Each type of device serves different needs and is chosen based on the required precision, budget, and intended use. The advantages and disadvantages of common technical solutions associated with personal and institutional devices are shown in Table 2.

DOI: 10.54254/2753-8818/53/20240196

Table 2. Comparison of advantages and disadvantages of different technical solutions.

		Description	Advantages	Disadvantages
Personal Devices	Light Scattering	Measure the light scattered by particles when illuminated by a laser. The intensity of scattered light is proportional to the particle concentration.	Offers real-time monitoring and portable options, making it suitable for both stationary and mobile measurements.	Can be affected by humidity and requires calibration; may not accurately measure the actual mass of particles without adjustments.
	Laser Diffraction	Use a laser to measure the light diffraction pattern caused by particles, which helps estimate the size distribution and concentration of PM2.5 in the air.	Useful for determining particle size distribution alongside concentration.	Can be complex to set up and operate, and is generally more suited for controlled environments or research applications.
Institutional Devices	Gravimetric Analysis	Involve collecting particles on a filter over a specific period, and then weighing the filter to determine the mass of particulate matter.	The reference method for PM2.5 measurement provides highly accurate mass measurements of particles.	Time-consuming, requires laboratory conditions and does not provide real-time data.
	Beta Attenuation Monitoring (BAM)	Measure the mass concentration of particulates by detecting the reduction in beta radiation passing through an air sample collected on a filter.	Provide continuous, real-time monitoring with high accuracy, commonly used in regulatory air quality monitoring stations.	Generally expensive and large, making it less suitable for personal use.
	Tapered Element Oscillating Microbalance	Measure the mass of particulate matter by detecting the change in frequency of an oscillating tapered element as particles accumulate on the filter.	Provide continuous, real-time data and is less susceptible to humidity effects compared to light scattering methods.	High cost and sensitivity to vibrations and external conditions can affect the accuracy.
	Chemical Analysis	Air samples are collected and analyzed chemically to identify not only the concentration but also the composition of PM2.5.	Provides detailed information about the particulate composition, which is critical for source apportionment studies.	Requires sophisticated laboratory equipment and techniques, and is not suitable for real-time monitoring.

Each of these technical methods has its own set of advantages and limitations, and the choice of method often depends on the specific requirements of the monitoring project, including accuracy, cost, operational complexity, and the need for real-time data versus detailed compositional analysis. Overall, institutional equipment tends to focus on methods that provide the accuracy and detail necessary for compliance with environmental regulations and in-depth research, while personal devices prioritize accessibility, ease of use, and immediate feedback on air quality conditions. Each type of equipment plays a crucial role in comprehensive air quality monitoring and management strategies.

Therefore, to balance the advantages and disadvantages of the aforementioned personal and institutional equipment, it is proposed to construct a small, cost-effective, easily-to-use platform for high-throughput accurate measurement of particles. Lens-less based digital holographic microscopy offers a specific way to reach the target. As a Gabor in-line digital holographic microscopy [9], it enables the recording and reconstruction of an optical field modulated by various factors such as scattering, refraction, absorption, and reflection from a biomedical or technical micro-object [10,11]. The

DOI: 10.54254/2753-8818/53/20240196

reconstructed complex data contains information about amplitude and phase, which is crucial for quantitative imaging. For the quantitative reconstruction of the lens-less microscopy, the post-reconstruction, and numerical propagation of the optical field to the focus plane, such as, the angular spectrum method [12] is the most common procedures. Because the hologram was captured outside the focus plane, thus the automatic determination of the focus plane is often involved [13], like Sobel based autofocusing approaches, now also integrated into deep learning frameworks [14]. Furthermore, the resolution of the lens-less microscope platform is mainly limited by the pixel size, which will need to be small enough to capture the dense Gabor holographic fringes of the PM2.5 without optical magnification [15]. Lens-less microscope platform will be an attractive option for high-throughput quantitative measurement of particles. In addition, through microscopic images, current particulate matter detection equipment can be realized such as the 2D dimensions of the PM.

2. Basic Principles

2.1. Basic reconstruction principles of in-line holography

Based on Gabor in-line holography [9], the traditional lens-less microscope platform as the typical in-line holography consists of a light source, a CCD camera, and a sample placed between them, preferably near the CCD [16]. In this simple-structure system, a diffraction pattern resulting from an object is directly recorded by a digital image sensor array without being optically imaged or magnified by any lens elements (Fig.1). These recorded diffraction patterns are then computationally reconstructed to form the real distribution of the object.

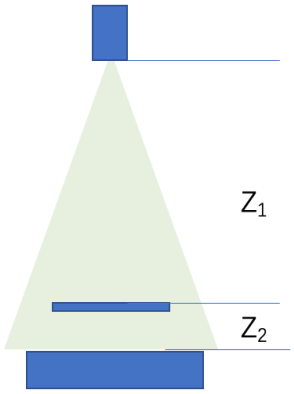

Figure 1. The structure of the lens-less microscope platform

Specifically, the patterns recorded on the sensor are the interference fringes (which can also be known as an in-line hologram) [9,17], which is generated by the interference between light scattered from an object on the sample and a reference wave that passes undisturbed through the transparent substrate [14]. The complex amplitude of the patterns can be denoted as:

$$\mathrm{U} = U_r + U_o = A_r + A_o(x,y)e^{i\phi(x,y)} \tag{1}$$

In this equation, U_r is the reference wave at the sample and U_o is the object wave at the sample. In Fig.1, a spherical wave of wavelength emanating from a "point" source of linear dimensions of the order of the wavelength, illuminates an object, typically a distance of a few thousand wavelengths from the source. Because the source-to-sample distance is much greater than the sample-to-sensor distance, the incident wave can be considered a plane wave over the range between the sample and sensor and A_r is the amplitude of the spatially uniform plane reference wave. $A_o(x,y)e^{i\phi_o(x,y)}$ is the spatially varying amplitude of the object, and $\phi_o(x,y)$ is the spatially varying phase of the object (which can be regarded as the optical thickness).

The aim of the in-line digital holographic reconstruction is to recover A_o and ϕ_o based on the images recorded by the sensor. With the angular spectrum approach, those measurements are possible to

DOI: 10.54254/2753-8818/53/20240196

reconstruct the amplitude and phase of the object [18]. This approach consists of computing the Fourier transform of the captured hologram, multiplying it by the transfer function of free space, and then inverse Fourier transforming [14]. Mathematically,

$$U_r = \mathscr{F}^{-1}\{\mathscr{F}\{U_H(x,y)\} \times H_{z_2}(x,y)\} \tag{2}$$

where U_r is the reconstructed optical field of the object, $I_H = [U_H(x,y)]^2$ is the captured hologram, and $H_{z_2}(x,y)$ is the transfer function of free space (assuming the refractive index of the medium is n = 1). z_2 is the sample-to-sensor distance, and $H_{z_2}(x,y)$ is:

$$H_{z_2} = \begin{cases} e^{ikz_2\sqrt{1-(\lambda f_x)^2-(\lambda f_y)^2}} & f_x^2 + f_y^2 < \frac{1}{\lambda^2} \\ 0 & f_x^2 + f_y^2 \geq \frac{1}{\lambda^2} \end{cases} \tag{3}$$

Here, λ is the wavelength of the light, f_x and f_y are spatial frequencies, and z_2 is the sample-to-sensor distance as shown in Fig. 1. Usually z_2 may not be precisely known before the capture of the hologram, and some computational "refocusing" can be performed to estimate it and provide the sharpest reconstructions.

2.2. Principle of the auto-focusing method

In our system, the whole process can be simplified as: a spherical wave of wavelength λ emanating from a "point" source illuminates the objects, and then a slightly magnified diffraction pattern will be recorded by the camera. The reason for the relatively small magnification here is that z_2 is much smaller than z_1. The captured diffraction pattern can be called a hologram, from which little information about the shape and structure of the object can be obtained by simple inspection.

In lensless microscopy, determining the optimal focal plane is crucial for obtaining high-resolution images. Traditional lens-based systems rely on adjustable lenses to achieve focus, but lensless systems must utilize computational methods. One effective technique for identifying the focal plane in lensless imaging is the Brenner Gradient method, which calculates a focus metric based on image intensity gradients.

The Brenner Gradient method is a widely used algorithm for autofocus in lensless microscopy. It operates by analyzing the intensity variations across an image to determine the sharpness, and consequently, the optimal focus. The fundamental principle of the Brenner Gradient method is that a well-focused image will exhibit higher intensity gradients compared to an out-of-focus image, where details are blurred.

To implement the Brenner Gradient method, the following steps are undertaken:

Step1: Image Acquisition

A series of images is calculated, and each image corresponds to a different plane in the three-dimensional space being examined. The calculated complex amplitude on different plane can be denoted as:

$$U_{cal} = \mathscr{F}^{-1}\{\mathscr{F}\{\sqrt{I_H(x,y)}\} \times H_{-z_2}(x,y)\} \tag{4}$$

Step2: Gradient Calculation

For each image $I_{cal} = |U_{cal}|^2$, the intensity gradients are calculated. This involves computing the difference in intensity values between adjacent pixels. The Brenner Gradient is defined mathematically as:

$$B(i,j) = I_{cal}(i+2,j) - I_{cal}(i,j) \tag{5}$$

where $I_{cal}(i,j)$ represents the intensity at pixel (i,j) in the image. This calculation is repeated for all pixels in the image.

Step3: Focus Metric Computation

DOI: 10.54254/2753-8818/53/20240196

The focus metric for each image is computed by summing the squares of the intensity differences obtained in the gradient calculation. This metric reflects the overall sharpness of the image. The formula for the focus metric FP is:

$$\mathrm{FP} = \sum_{i=1,j=1}^{M,N} [I_{cal}(i+2,j) - I_{cal}(i,j)]^2 \quad (6)$$

A higher value of FPindicates a sharper image. Here M,N represents the number of horizontal and vertical pixels used to calculate the region image, respectively.

Step4: Optimal Focus Determination

By comparing the focus metrics of all captured images, the image with the highest focus metric is identified as the best-focused image. This image represents the optimal focal plane.

Step5: Image Reconstruction

Once the optimal focal plane is determined, the defocusing distance can be obtained. The angular spectrum method will be used for the reconstruction [12].

3. System design and construction

3.1. Overall light path system design

The diagram (Fig.2) below illustrates the light path of the digital microscope, starting with an LED that provides a stable source of light. This light illuminates the sample which can be a slide or a sample collection device [here is the air-o-cell as shown in Fig.2(b)], and the air pump will pump the air into the air-o-cell to examine. Finally, the interaction between the light and the sample is captured by the camera.

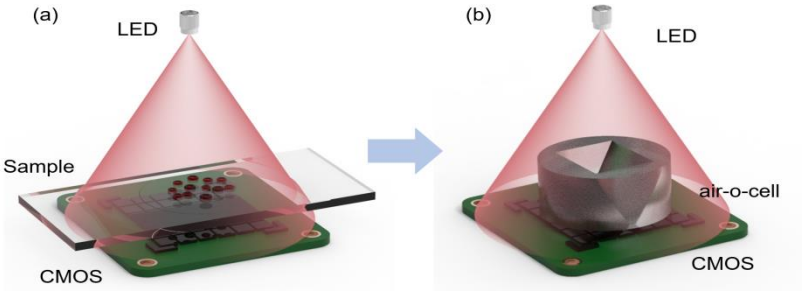

Figure 2. Schematic diagram of system optical path structure

3.2. Hardware selection

The whole system contains a total of six components, mainly including the outer shell, CMOS, air-o-cell, air pump, LED and the micro control unit (Arduino). In order to reduce the size of the entire system, KY-009 LED [Fig.3(a)] is selected as the light source, which can emit light of three different wavelengths: red, green, and blue. Only one wavelength is utilized in this system. The use of three wavelengths can improve the reconstruction quality and is also a direction for future upgrades of this system. Arduino UNO R3 microcontroller [Fig.3(b)] is used to drive the illumination of the LED. To connect the LED with the microcontroller, the three positive and GND wires of the LED are directly connected to the number 11~12 and GND ports in the microcontroller. By programming the microcontroller to control the related output in different ports, the LED can be controlled. The air-o-cell is directly placed on the CMOS. The air pump (AQQA aquarium air pump, Fig.3(d)) will deliver ambient gas to the air-o-cell [Fig.3(c)] at a speed of 1.7L/min. The part in the red circle of Fig.3(d) has been manually removed. The compressed air speed can be changed to different air pump models according to demand to achieve any speed of gas delivery. The air-o-cell is a specialized air sampling device designed for the efficient and rapid collection of a diverse array of airborne particles. It captures pollen, insect parts, skin cell fragments, mold spores, various fibers (such as asbestos, cellulose, fiberglass and clothing fibers), and inorganic particulates like fly ash, ceramic and copier toner [19]. This device is capable of collecting both viable and non-viable specimens, offering a more comprehensive analysis of

DOI: 10.54254/2753-8818/53/20240196

potential allergens and contaminants compared to traditional methods. The air-o-cell operates based on the principle of inertial impaction. When air containing particulate matter is drawn through the cassette's tapered inlet slit, it accelerates and is directed towards a slide with a sticky collection medium. The particles impact and adhere to the slide, while the clean air exits through the outlet. The adhesive properties of the collection medium ensure that particles remain in place during laboratory processing, preventing blurring and loss of samples due to handling and transportation vibrations. The output wire of the CMOS can be directly connected to the computer to record the picture captured. The CMOS type is the imaging source DMM 27UJ003-ML [No-Mount, Fig.3(e)], with resolution 3872px × 2764px, pixel Size (H×V) 1.67μm × 1.67μm, frame rate 14 fps, and mono color. These hardware devices will be assembled using 3D printed shells, as shown in Fig3(f). Please refer to the next section for details.

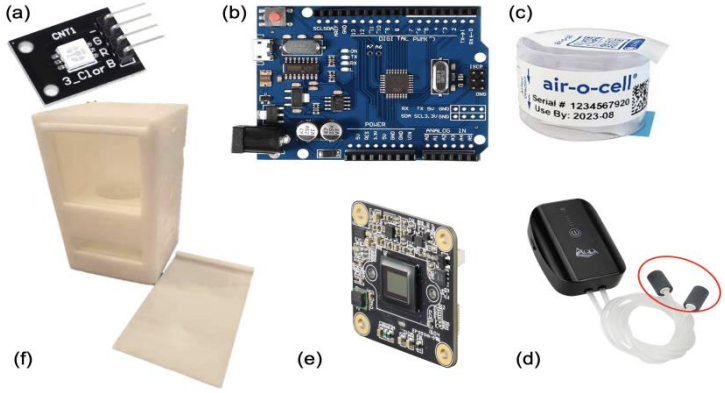

Figure 3. The hardware used in this system

3.3. D prototype building

Due to the scattering angle of the light source when illuminating the sample, theoretically, the farther the light source is from the surface of the camera sensor, the larger the range of illumination, as shown in Fig. 1. In addition to the large scattering angle of the LED, the narrow of spectral width can be provided. According to the official manual, the spectral widths of the three channels in RGB are 620-625nm, 520-525nm, 465-470nm. In this system, in order to measure PM2.5 in this system, with a half width resolution of at least 2.5 microns, we can calculate the temporal coherence (spectral width) of the light source in reverse using the following Eq. 7 [20]. In this system, the temporal coherence (spectral width) of the light source will not affect the imaging resolution when the defocus distance is less than 0.01 meters.

$$q = \sqrt{\frac{z_{2\Delta\lambda}}{8}} \tag{7}$$

In addition, we also need to consider the spatial coherence of the light source. Based on the direct impact of the coherence and resolution of the light source, as well as the size of the light source, in order to avoid the influence of the coherence of the light source as much as possible, the source-sample distance z_1 may be increased, and the sample-sensor distance $z_2$may be minimized. The size of the source Δs should be as small as possible. But after selecting the LED model here, the size is basically fixed ($\Delta s = 250\mu m$), and the one that can be changed is z_1 and z_2. The relationship between these parameters can be noted as [20]:

$$q = \frac{z_{2\Delta s}}{2z_1} \tag{8}$$

Considering that the distance between the collection location of air-o-cell products and the sensor generally does not exceed 1.6mm, and that Eq. 8 must be met, the final source to sensor distance is determined to be 95mm. When designing 3D printed shells, it is important to try to do so as much as possible.

DOI: 10.54254/2753-8818/53/20240196

For the outer shell, the 3D printing material is polylactic acid or polylactide (PLA). The KY-009 LED is used in this system because of its small size. Furthermore, this LED is used since it can separately control all three RGB values, and the distance between three small LEDs is in an acceptable range. In order to assemble the system, the air-o-cell should be limited to the center of the system's optical path, and it should also be as close to the sensor as possible. In addition, a small hole needs to be opened on the side for the air pump to extract air and deliver it to the air-o-cell inside the system. The CMOS and its supporting components should be fixed with a screw and nut. The wire should be appropriately carried out by drilling holes in the supporting component. Finally, assemble the slide cover with the main supporting component, and do the first test of the system. Considering the basic experimental conditions and cable routing, the final size for 3D printing is determined to be $72 \times 72 \times 140mm$, as shown in Fig. 4.

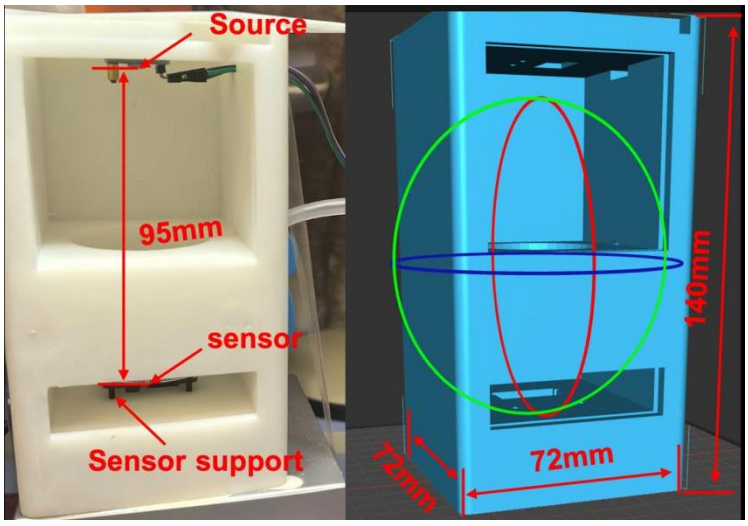

Figure 4. Appearance design of the system (The system also has a side cover that is not displayed)

4. Experiment

4.1. USAF Resolution Board (Quantitative experiment)

In order to test performance of the system, the USAF resolution board will be used to test the resolution of the system and roughly display the experimental result processing procedure. There are several steps to be done throughout the process (aftering taking the background image):

1. Capture the raw image as shown in Fig.5(a).
2. Selecting a portion of the image. For example, we selected the center region of Fig.5(a), which is shown in Fig.5(b). Here the entire Fig.5(a) can be imported into the program for calculation. Only a part of it is selected here to reduce the computational load on the computer.
3. Apply the Brenner gradient algorithm to the image for autofocusing (See the section 3.2). The Brenner gradient algorithm measures image sharpness by calculating the first-order differences of the image. Specific steps include:

- Compute the gradient value for each pixel of the image.
- Aggregate the overall gradient values of the image.
- Select the focal point with the maximum gradient value as the best focus.

For our system and the USAF resolution target, the curve of the auto-focusing is shown in Fig. 5(c). The graph shows the clarity of different positions, and the highest means the clearest. The maximum gradient value appears at the position 99. Since we start from $300\mu m$ and search for the focusing position in $1\mu m$ steps, the actual distance corresponding to position 99 is $399\mu m$.

DOI: 10.54254/2753-8818/53/20240196

4. After obtaining the defocus distance, we use the angular spectrum propagation model for backpropagation to obtain the distribution at the focal position, as shown in Fig. 5(d).

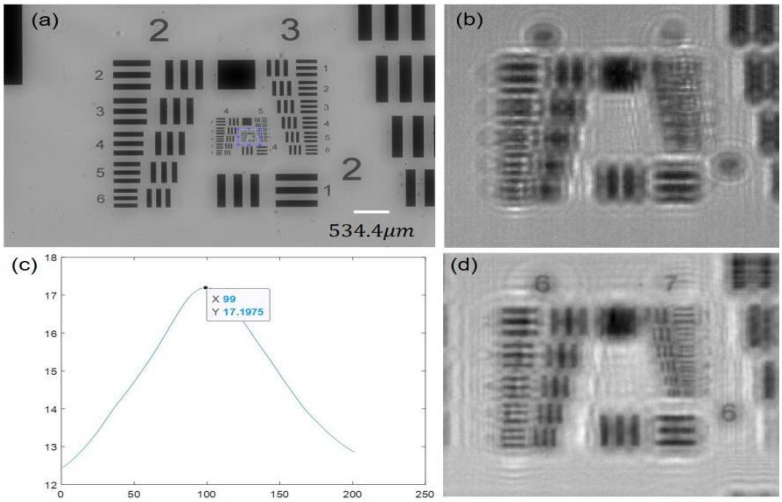

Figure 5. The reconstruction of the USAF resolution board

Fig.5(b) and Fig.5(d) separately display the distribution of objects in the same area before and after auto-focusing with the Brenner gradient algorithm. The comparison indicates that the reconstructed image (Fig.5(d)) is clearer in detail, with enhanced contrast at the edges. In Fig.5(d), it can be found that the element six of the group 7 is recovered, which means that the half-pixel resolution can be reach $2.192\mu m$. This resolution is sufficient for us to observe particles in the air. It should be noted that compared to the field-of-view with a traditional high-magnification microscope, the background of the reconstruction shown in Fig.5(d) is relatively "dirty", mainly because we only used single-frame reconstruction, resulting in the presence of conjugate images. In the future, three wavelengths may be used to reduce conjugate images.

4.2. Plastic Ruler

Since the substrate of the USAF standard resolution target is glass, the reconstructed results are relatively ideal. To better approximate the subsequent PMs measurement experiments, we used a plastic ruler with lower transparency as a sample to verify that the system can still achieve reconstruction for non-standard experimental objects.

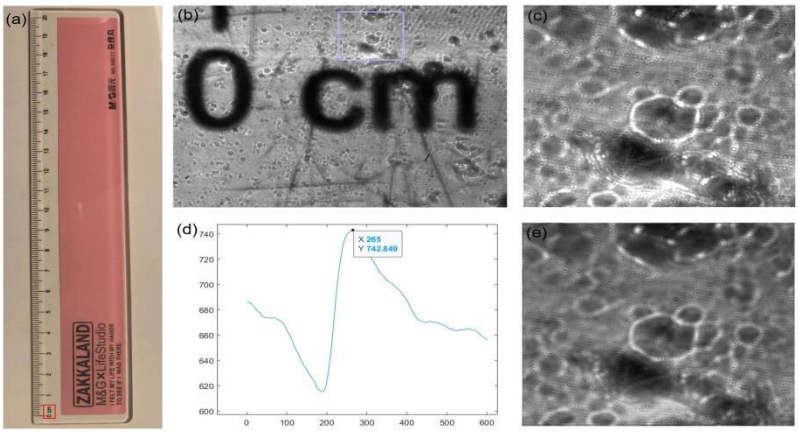

Figure 6. The reconstruction of the plastic ruler

DOI: 10.54254/2753-8818/53/20240196

For the plastic ruler, the reconstruction and processing procedures are the same as in section 5.1. Fig.6(a) is the picture of the ruler, and Fig.6(b) is the raw captured image which corresponds to the red-rectangular area of Fig.6(a). The blue-rectangular area of Fig.6(b) The blue area was selected for further processing. The selected region can be freely chosen based on the positions of interest, and the size of the selected area mainly depends on the computer's configuration and the acceptable processing time. Fig.6(c) is the magnified image of the blue-rectangular area of Fig.6(b). The curve of the auto-focusing of this chosen portion is shown in Fig. 6(c). The maximum gradient value appears at the position 265. In the code, we start from $200\mu m$ and search for the focusing position in $1\mu m$ steps, the actual defocusing distance corresponding to position 265 is $465\mu m$.

4.3. PMs

To reduce the replacement of the air-o-cell and extend its service life, we use two measurements to lower the replacement frequency of the air-o-cell. The specific connections, including the light source, air pump, and camera, are shown in Fig.7. Here the air pump can be replaced with different models according to actual needs.

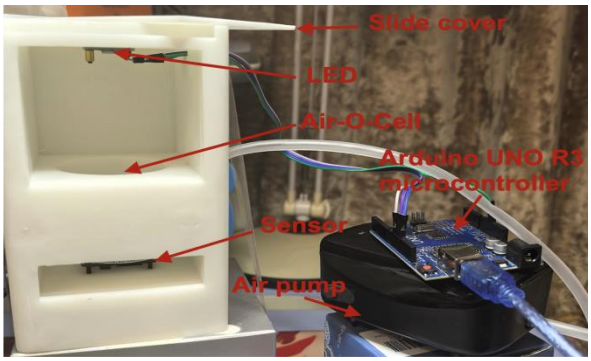

Figure 7. Photo of the entire experimental system (the side cover needs to be closed during the experiment)

The collection and processing process can be as follows:

1. Place the air-o-cell on the sensor, its horizontal position has been determined during 3D printing. After placement, obtain an original image as the starting state. Capture the raw image as shown in Fig.8(a).
2. Turn on the air pump. The opening time can be autonomously selected based on the flow rate of the air pump and the ambient air quality. In our experiment, the air pump flow rate is 1.7L/min, and the opening time is 10 minutes.
3. Turn off the air pump, and capture the image as shown in Fig.8(b).
4. Then the same regions of Fig.8(a) and Fig.8(b) are selected for reconstruction (The white rectangular area). Select one area for analysis, and the enlarged image of the selected area is shown in Fig.8(a1) and Fig.8(b1). The reason for selecting the area for calculation here is mainly because if the entire field graph is used for calculation, the computer load will be too high. Divide the entire map into parts for calculation.
5. For our system, the curve of the auto-focusing is shown in Fig.9. The maximum gradient value appears at the position 74. Since we start from $350\mu m$ and search for the focusing position in $1\mu m$ steps, the actual distance corresponding to position 74 is $423\mu m$.
6. With the calculated de-focusing distance, the reconstructions corresponding to Fig.8(a1) and Fig.8(b1) are shown in Fig.8(a2) and Fig.8(b2) respectively. Comparing Fig.8(a2) and Fig.8(b2), the impurity pointed to by the arrow in Fig. 8(b2) is something newly added during this 10-minutes period. The reconstruction of the entire field-of-view (corresponding to Fig.8(b)) is shown in Fig.9(b).

DOI: 10.54254/2753-8818/53/20240196

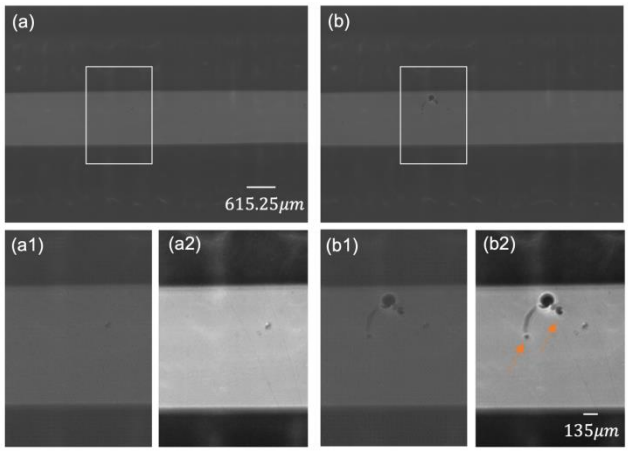

Figure 8. The reconstruction of the PMs (the selected small area).

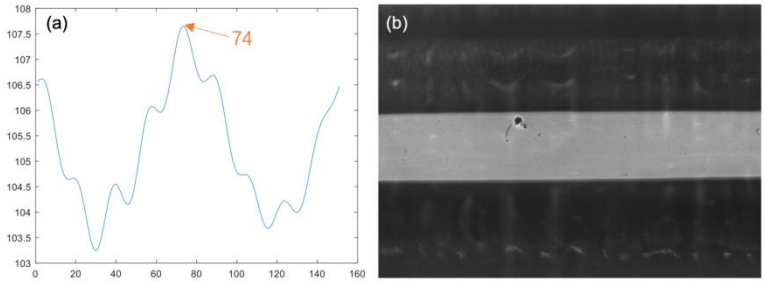

Figure 9. (a) The curve of the auto-focusing. (b)The reconstruction of the entire field-of-view.

4.4. Data analysis

In order to further analyze the imaging results of the system, the reconstruction results corresponding to Fig.8(b) and Fig.8(a) were subtracted, and the result is shown in Fig.10. The newly added matters are the particles matters in the 17L volume of air.

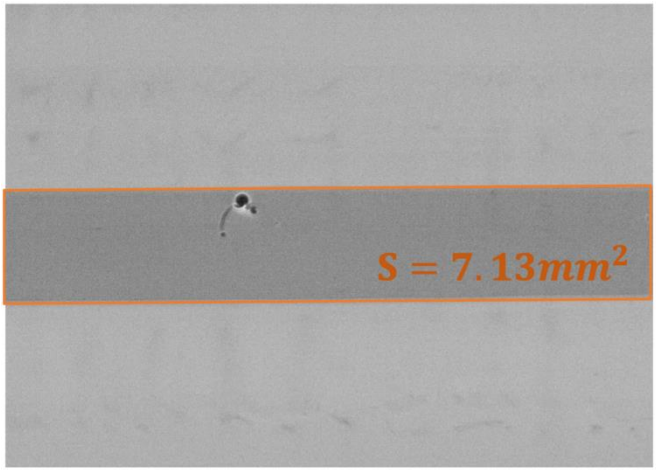

Figure 10. Within the entire field-o-view, PMs are added in 10 minutes.

In this experiment, the density of the particles matters is low, so it is necessary to select all areas that can collect particles and finally calculate the added particles as the shown in Fig.10. The effective calculated area in the experiment is shown in the orange rectangular area in the Fig.10. When the density

DOI: 10.54254/2753-8818/53/20240196

is high, statistical estimation only needs to be made based on the size of the selected reconstruction area and its large proportion in the collection area. In Fig.5(d), the element six of the group 7 can be recovered, which means that $2.192\mu m$ sized particles can be observed. We did not capture such small particles during the 10-minute-measurement period. It is difficult to quickly determine the size of the collected particles using traditional methods, which also reflects an advantage of lensless imaging in measuring PMs.

This is the result of static measurement. If necessary, the entire process can be recorded at the highest frame rate of the camera, and a reconstruction result can be obtained for each frame. These reconstruction results can dynamically display the dynamic distribution of PMs.

5. Conclusion

Air quality monitoring is vital for health, but detecting airborne particulate matter (PM), especially PM2.5, is challenging due to pollution and distribution issues. PM2.5 particles, with diameters less than 2.5 micrometers, have significant health impacts. Traditional PM detection methods are often slow or require complex optical systems. This study investigates lensless microscopy as an innovative, cost-effective alternative for visualizing and measuring PMs. Using computational imaging, lensless microscopy captures high-resolution images without traditional lenses, enabling rapid and accurate air quality analysis. Our implementation of lensless imaging for detecting and quantifying PM2.5 demonstrated effective capture of fine PM details, achieving resolutions comparable to traditional microscopy. This validates lensless microscopy as a practical tool for real-time air quality monitoring. By adjusting the air pump flow rate, PM measurement speed can be adapted to different environments. This research presents a novel, efficient, and economical approach to air quality assessment, offering a promising solution for rapid, detailed PM analysis at an affordable cost.

Of course, from the reconstruction results, we can obtain the distribution of the object on the focal plane, but there are oscillations around the object, which is physically called conjugate images. This is mainly because our results were obtained through single frame reconstruction, and in subsequent improvements, we consider collecting and calculating the distribution of objects at other wavelengths to suppress these images.

References

[1] "Particulate Matter (PM) Basics." *EPA*, Environmental Protection Agency, www.epa.gov/pm-pollution/particulate-matter-pm-basics#PM. Accessed 20 Aug. 2024.

[2] "Household Air Pollution." *World Health Organization*, www.who.int/news-room/fact-sheets/detail/household-air-pollution-and-health?gad_source=1&gclid=Cj0KCQjwudexBhDKARIsAI-GWYV1MZ4mkioBSTdoSssM1711NAKfiWT8T9ahtgQ6Q_43u6azN4w7qzYaArMlEALw_wcB. Accessed 20 Aug. 2024.

[3] Morakinyo, Oyewale Mayowa, et al. "Health outcomes of exposure to biological and chemical components of inhalable and respirable particulate matter." International journal of environmental research and public health 13.6 (2016): 592.

[4] Air Monitoring for Fine Particle Pollution (PM2.5) Fact Sheet, www.epa.gov/system/files/documents/2024-02/pm-naaqs-monitoring-fact-sheet.pdf. Accessed 20 Aug. 2024

[5] "NEW WHO Global Air Quality Guidelines Aim to Save Millions of Lives from Air Pollution." *World Health Organization*, www.who.int/news/item/22-09-2021-new-who-global-air-quality-guidelines-aim-to-save-millions-of-lives-from-air-pollution. Accessed 20 Aug. 2024.

[6] "Monitoring Air Pollution Levels Is Key to Adopting and Implementing Who's Global Air Quality Guidelines." *World Health Organization*, www.who.int/news/item/10-10-2023-monitoring-air-pollution-levels-is-key-to-adopting-and-implementing-who-s-global-air-quality-guidelines. Accessed 20 Aug. 2024.

[7] "Ambient (Outdoor) Air Pollution." *World Health Organization*, www.who.int/news-room/fact-sheets/detail/ambient-(outdoor)-air-quality-and-health. Accessed 20 Aug. 2024.

DOI: 10.54254/2753-8818/53/20240196

[8] "Particulate Matter Monitoring Market Size, Share, Trends 2033." *MarketsandMarkets*, www.marketsandmarkets.com/Market-Reports/particulate-matter-monitoring-market-153413567.html. Accessed 20 Aug. 2024.
[9] Gabor, Dennis. "A new microscopic principle." (1948): 777-78.
[10] Kemper, Björn, and Gert Von Bally. "Digital holographic microscopy for live cell applications and technical inspection." Applied optics 47.4 (2008): A52-A61.
[11] Takeda, Mitsuo, Hideki Ina, and Seiji Kobayashi. "Fourier-transform method of fringe-pattern analysis for computer-based topography and interferometry." *JOSA* 72.1 (1982): 156-160.
[12] Zhang, Yibo, et al. "Edge sparsity criterion for robust holographic autofocusing." Optics letters 42.19 (2017): 3824-3827.
[13] Wu, Yichen, et al. "Extended depth-of-field in holographic imaging using deep-learning-based autofocusing and phase recovery." Optica 5.6 (2018): 704-710.
[14] Ozcan, Aydogan, and Euan McLeod. "Lensless imaging and sensing." Annual review of biomedical engineering 18 (2016): 77-102.
[15] Vashist, Sandeep Kumar, et al. "Cellphone-based devices for bioanalytical sciences." Analytical and bioanalytical chemistry 406 (2014): 3263-3277.
[16] Agbana, Temitope E., et al. "Aliasing, coherence, and resolution in a lensless holographic microscope." Optics letters 42.12 (2017): 2271-2274.
[17] Göröcs, Zoltán, and Aydogan Ozcan. "On-chip biomedical imaging." IEEE reviews in biomedical engineering 6 (2012): 29-46.
[18] Goodman J. 2004. Introduction to Fourier Optics. Greenwood Village, CO: Roberts. 491 pp. 3rd ed.
[19] "Air-O-Cell Bioaerosol Sampling Cassette - Operating & Instruction Manual.", *Zefon International*, www.zefon.com/airocell-user-manual. Accessed 20 Aug. 2024.
[20] Zhang, Jialin, et al. Resolution analysis in a lens-free on-chip digital holographic microscope." IEEE transactions on computational imaging 6 (2020): 697-710.